

Carrier Localization on the Nanometer-Scale limits Transport in Metal Oxide Photoabsorbers

Markus Schleuning, Moritz Kölbach, Ibbi Ahmet, Raphael Präg, Ronen Gottesman, René Gunder, Mengyuan Zhang, Dan Ralf Wargulski, Daniel Abou-Ras, Daniel A. Grave, Fatwa F. Abdi, Roel van de Krol, Klaus Schwarzburg, Rainer Eichberger, Dennis Friedrich,* and Hannes Hempel*

Metal oxides are considered as stable and low-cost photoelectrode candidates for hydrogen production by photoelectrochemical solar water splitting. However, their power conversion efficiencies usually suffer from poor transport of photogenerated charge carriers, which has been attributed previously to a variety of effects occurring on different time and length scales. In search for common understanding and for a better photo-conducting metal oxide photoabsorber, CuFeO_2 , $\alpha\text{-SnWO}_4$, BaSnO_3 , FeVO_4 , CuBi_2O_4 , $\alpha\text{-Fe}_2\text{O}_3$, and BiVO_4 are compared. Their kinetics of thermalization, trapping, localization, and recombination are monitored continuously 100 fs–100 μs and mobilities are determined for different probing lengths by combined time-resolved terahertz and microwave spectroscopy. As common issue, we find small mobilities $< 3 \text{ cm}^2\text{V}^{-1}\text{s}^{-1}$. Partial carrier localization further slows carrier diffusion beyond localization lengths of 1–6 nm and explains the extraordinarily long conductivity tails, which should not be taken as a sign of long diffusion lengths. For CuFeO_2 , the localization is attributed to electrostatic barriers that enclose the crystallographic domains. The most promising novel material is BaSnO_3 , which exhibits the highest mobility after reducing carrier localization by annealing in H_2 . Such overcoming of carrier localization should be an objective of future efforts to enhance charge transport in metal oxides.

1. Introduction

Metal oxides (MOs) are widely used as active materials in optoelectronics,^[1] sensors,^[2,3] catalysis, for example, for CO_2 reduction,^[4] and solar energy conversion.^[5] This work focuses on metal oxides developed for photoelectrochemical (PEC) hydrogen production from water by solar illumination as CO_2 -free and storable energy production is considered a key element of a fully sustainable economy.^[6,7] These metal oxides are usually proposed for direct solar water splitting, which promises possible cost reduction from better integration and improved heat management compared to indirect solar water splitting using photovoltaic-powered electrolyzers.^[8] The main advantages of metal oxides such as TiO_2 ,^[9] $\alpha\text{-Fe}_2\text{O}_3$,^[7] and BiVO_4 ^[10] over conventional non-oxide semiconductors can be their earth-abundance, non-toxicity, ease of preparation, and better stability in aqueous solution.

M. Schleuning, M. Kölbach, I. Ahmet, R. Präg, R. Gottesman, F. F. Abdi, R. van de Krol, K. Schwarzburg, R. Eichberger, D. Friedrich
Institute for Solar Fuels
Helmholtz-Zentrum Berlin für Materialien und Energie GmbH
Hahn-Meitner-Platz 1, 14109 Berlin, Germany
E-mail: friedrich@helmholtz-berlin.de

M. Schleuning, R. Präg, R. Gottesman, R. van de Krol
Institut für Chemie
Technische Universität Berlin
Straße des 17. Juni 124, 10623 Berlin, Germany

M. Kölbach
Institute of Physical and Theoretical Chemistry
Universität Tübingen
Auf der Morgenstelle 15, 72076 Tübingen, Germany

 The ORCID identification number(s) for the author(s) of this article can be found under <https://doi.org/10.1002/adfm.202300065>.

© 2023 The Authors. Advanced Functional Materials published by Wiley-VCH GmbH. This is an open access article under the terms of the Creative Commons Attribution License, which permits use, distribution and reproduction in any medium, provided the original work is properly cited.

DOI: 10.1002/adfm.202300065

R. Gottesman
The Institute of Chemistry
The Hebrew University of Jerusalem
Edmond J. Safra Campus, Givat Ram, Jerusalem 9190401, Israel

R. Gunder, D. R. Wargulski, D. Abou-Ras, H. Hempel
Department Structure and Dynamics of Energy Materials
Helmholtz-Zentrum Berlin für Materialien und Energie GmbH
Hahn-Meitner-Platz 1, 14109 Berlin, Germany
E-mail: hannes.hempel@helmholtz-berlin.de

M. Zhang
School of Materials Science and Engineering
Nanyang Technological University
Singapore 639798, Singapore

D. A. Grave
Department of Materials Science and Engineering
Technion – Israel Institute of Technology
Haifa 3200003, Israel

D. A. Grave
Department of Materials Engineering
Ben-Gurion University of the Negev
David Ben Gurion Blvd 1, Be'er Sheva 8410501, Israel

However, the demonstrated solar to hydrogen (STH) conversion efficiencies of devices fully based on metal oxides are commonly limited to $\approx 1\%$,^[11,12] while the latest record of 3% was achieved with a $\text{Cu}_2\text{O}/\text{BiVO}_4$ tandem.^[13] Tandems with silicon or III-V bottom cells have achieved STH efficiencies of up to 8.1%,^[14] but are also limited by the metal oxide top cell. The poor STH efficiency in current metal oxide-based devices has been partially attributed to poor charge transport in previous works,^[6,15–19] which motivates our investigation of the origin of this poor charge transport and our search for novel metal oxides with possibly superior charge transport properties.

Therefore, we probe the mobility and charge transport of several metal oxides, established and novel, such as $\alpha\text{-Fe}_2\text{O}_3$,^[20] $\alpha\text{-SnWO}_4$,^[21] CuFeO_2 ,^[22] FeVO_4 ,^[23] BiVO_4 ,^[24] CuBi_2O_4 ,^[25] and BaSnO_3 .^[26] To this end, photoconductivity transients are detected from 100 fs up to 100 μs by an innovative combination of time-resolved microwave conductivity and optical-pump terahertz-probe spectroscopy, which allows continuous and rather complete monitoring of the kinetics of thermalization, trapping, localization, and recombination of charge carriers in these materials. All metal oxides probed here, except BiVO_4 , show distinct signs of carrier localization on the nanometer scale, which poses additional transport losses. Further, we can show that modifications of the materials can reduce the carrier localization in some cases, which rationalizes increased photocurrents that have been observed previously.

The first aspect of carrier localization that will be discussed here is the offset between OPTP and TRMC transients and decreasing mobility with decreasing probing frequency. Second, a model of carrier localization is developed using CuFeO_2 as an example, which integrates the carrier localization length, the probing lengths by TRMC and OPTP, the XRD domain size, and the Debye length at electrostatic potential barriers. Thirdly, the overestimation of the diffusion length in the presence of carrier localization is discussed, which occurs when the mean absolute displacement increases beyond the probing lengths of TRMC and OPTP. Finally, a comparison of various metal oxides reveals their common issue of intrinsically low mobilities compared to high-efficiency photoabsorbers such as silicon and III-V semiconductors and that nm-scale localization further reduces their mobilities.

2. Carrier Localization in CuFeO_2

Before comparing various metal oxides, we detail our approach on the example of delafossite rhombohedral CuFeO_2 . This material has recently been proposed as a candidate metal oxide for solar water splitting as it has a suitable bandgap in the visible range ($E_g \approx 1.4$ eV) and intrinsic p-doping, which is favorable for a photocathode.^[22,27] The so far limited investigation of the charge carrier dynamics of CuFeO_2 (e.g., no OPTP study) and the distinct carrier localization behavior, make it a perfect candidate for a more detailed study.

2.1. Combined Photoconductivity Transients and Initial Mobility

To span different time-windows, photoconductivity transients are measured after pulsed photogeneration by OPTP, sample

terminated (st)-TRMC, open cavity (oc)-TRMC, and conventional TRMC, and are combined in **Figure 1a**. The excitation wavelength was set at 410 and 400 nm for TRMC and OPTP, respectively, while the number of exciting photons per pulse was in the order of $\approx 5 \times 10^{13} \text{ cm}^{-2}$ as detailed in Supporting Information^{80–85}. The OPTP and TRMC photoconductivity transients have been divided by the initial photogenerated carrier concentrations and the elementary charge, which allows direct determination of the charge carrier mobility from the peak value in units of $\text{cm}^2\text{V}^{-1}\text{s}^{-1}$. This value is the sum of the electron mobility and the hole mobility, because TRMC and OPTP measure the photoconductivity of both carrier types. Instead, the st- and oc-TRMC transients are in arbitrary units as the cavity resonance is not well defined. These transients can, therefore, be stitched to the OPTP transient or the conventional TRMC transient.

The kinetics of the individual transients match well in the overlapping time regimes, which provides confidence that the individual techniques probe the same charge carrier ensemble. However, to obtain a continuous photoconductivity transient, the OPTP transient must be divided by a divisor of ≈ 14 . This discontinuity in the transient can be attributed to a frequency-dependence of the probed charge carrier mobility. OPTP uses electric fields that alternate at ≈ 1 THz, whereas the TRMC setup uses ≈ 9 GHz. From the initial amplitude of the OPTP transient in **Figure 1a** (at $t \approx 100$ fs, measured using a probe frequency of ≈ 1 THz), a mobility of $0.43 \text{ cm}^2\text{V}^{-1}\text{s}^{-1}$ at ≈ 1 THz is found. Stitching the adjusted OPTP and st/oc-TRMC transients to the TRMC data (i.e., dividing the OPTP transient by a factor of 14) provides an extrapolation of $0.029 \text{ cm}^2\text{V}^{-1}\text{s}^{-1}$ for the initial mobility at 9 GHz. In contrast, the TRMC-derived peak mobility is only $6.2 \times 10^{-4} \text{ cm}^2\text{V}^{-1}\text{s}^{-1}$ due to a photoconductivity decay within TRMC time resolution of ≈ 10 ns, which has been previously described also for BiVO_4 and amorphous silicon.^[28]

It is interesting to note that in our previous work on bismuth vanadate, amorphous and single crystalline silicon, and halide perovskites no offsets between OPTP and TRMC transients were observed.^[28] These materials exhibit approximately constant mobilities between 9 GHz and 1 THz, which is in line with free-carrier Drude-like transport but also with hopping between lattice sites or partial carrier localization on atomistic length scales.^[29] In contrast, the observed decreasing mobility with decreasing frequency for CuFeO_2 (a factor of 14 between 1 THz and 9 GHz) indicates charge carrier localization on the nanometer scale.^[30–32] Such reduced GHz mobilities have been reported previously for $\alpha\text{-SnWO}_4$ ^[33] and certain MAPbI_3 thin films^[34] and were attributed to transport barriers at grain boundaries. Thus, a modification of our previously reported carrier transport model^[28] is necessary to represent this effect, which is discussed below.

2.2. Mobility Dispersion by Carrier Localization

The frequency dependence of the mobility in the THz range can be investigated in more detail by time-resolved terahertz spectroscopy (TRTS), a modification of OPTP. The terahertz mobility spectrum of CuFeO_2 was measured by TRTS at 5 ps after photogeneration and is shown in **Figure S5** (Supporting

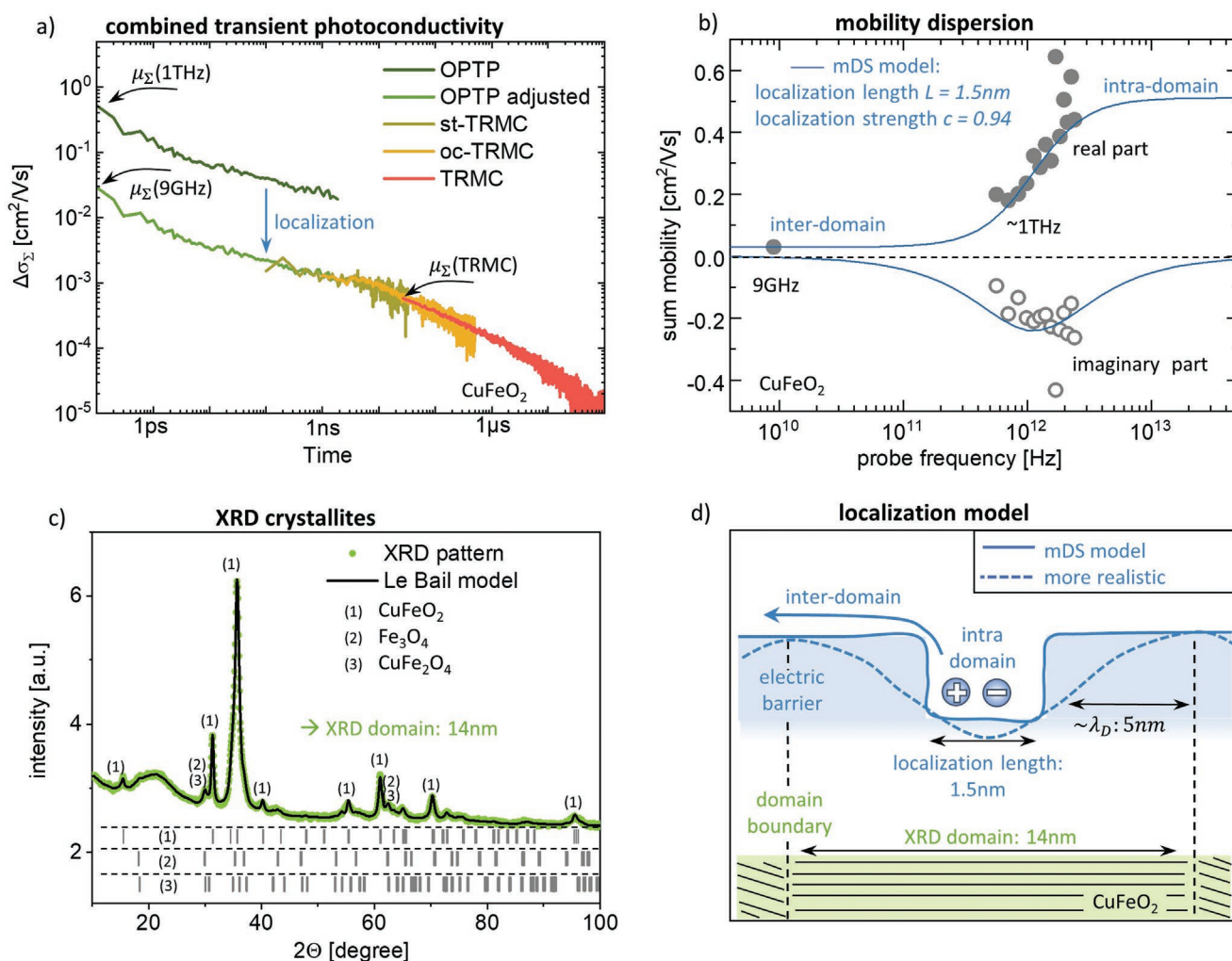


Figure 1. Carrier localization on nanometer-scale in CuFeO₂. a) Combined photoconductivity transient of a CuFeO₂ thin film. TRMC transient and OPTP transient are offset by a factor, which can be attributed to reduced TRMC mobility by charge carrier localization. b) Frequency-dependent mobility spectrum of CuFeO₂ measured by time-resolved terahertz spectroscopy at 5 ps and by TRMC. The THz and GHz mobilities are scaled to the peak values observed in a) and fitted by the modified Drude–Smith model. One finds a localization length L of 1.5 nm, a localization strength c of 0.94, and an intra-domain carrier mobility μ_0 of $0.51 \text{ cm}^2\text{V}^{-1}\text{s}^{-1}$. c) X-Ray diffractogram of CuFeO₂. An average domain size $< 14 \text{ nm}$ is extracted via the Le Bail method. d) Illustration of carrier localization in the potential well of the modified Drude–Smith model and more realistic between electric barriers from crossed XRD-domain boundaries, which decay with the Debye-length λ_D toward to domain center.

Information). In Figure 1b, this data is scaled to the THz peak mobility and plotted together with the respective mobility at 9 GHz. The real part of the mobility decreases with decreasing frequency, while the imaginary part of the mobility is negative, typical for carrier localization.^[35,36] Such mobility dispersion has been described previously by various localization models, such as the Drude Smith model^[37–39] or by hopping transport.^[40] In this work, the modified Drude–Smith (mDS) model is used, which describes carrier localization in a potential well as illustrated in Figure 1d.^[32,35] The first reason for choosing this model is that it can model transport within localizing domains without assuming that the charge carrier scattering is dominated by the domain boundaries, which is implied in the original Drude–Smith model. Second, it can phenomenologically describe transport between localizing domains by the inclusion of parameter c , which we will call “localization strength”. This

parameter is not included in the otherwise similar Siebbeles model.^[41] Thirdly, the mDS-model considers the spatial extent L_{loc} of the localizing domain, which we will call “localization length” and will be compared later to the morphology of the probed polycrystalline thin films. If the localization length is longer than the intra-domain scattering length, the mDS-model can be expressed as Equations 1 and 2:

$$\mu_{mDS}(f) = \mu_0(f) \left(1 - \frac{c}{1 - i2\pi f\tau''} \right) \quad (1)$$

$$\tau'' = \frac{eL_{loc}^2}{12k_B T \mu_0(f=0)} \quad (2)$$

where μ_0 is the intra-domain mobility, which was originally described by Cocker et al. as a free-carrier Drude mobility

spectrum. Without proof, we suggest that the intra-domain mobility could possibly also be described by other models, for example, hopping, depending on the intra-domain transport. f is the probing frequency and τ'' can be understood as the time to diffuse through the localizing domain. k_B , T and e are the Boltzmann constant, temperature, and elementary charge, respectively. More details of the model are explained in Supporting Information.

Modeling the combined THz and GHz mobility spectrum (Figure 1b) with these equations yields a localization length L_{loc} of 1.5 nm, a localization strength c of 0.94, and an intra-domain carrier mobility μ_0 of $0.51 \text{ cm}^2\text{V}^{-1}\text{s}^{-1}$, which is approached above ≈ 5 THz. This intra-domain mobility can, for example, be described by a Drude-like free-carrier mobility with an effective mass $m_{eff} = 1$ and scattering time $\tau_{scat} = 0.29$ fs. However, other combinations of effective mass and scattering time can also be used to model the measured data; for an unambiguous determination, a measurement at higher THz frequencies would be needed.

The localization strength c is a phenomenological extension in the modified Drude–Smith model to its rigid deviation. It allows transport beyond the individual localization domains with an inter-domain mobility that is reduced to $(1-c)\mu_0$. The localization parameter scales, as defined here, from 0 for the absence of localization to 1 for complete localization in the domain with an inter-domain mobility reduced to zero. The relatively large localization strength of 0.94 for CuFeO_2 indicates that the barriers at the boundaries of the localization domains are relatively high compared to the thermal energy of the charge carriers and cannot be overcome easily. It reduces the mobilities at lower frequencies, which have approached an inter-domain value $(1-c)\mu_0$ of $0.029 \text{ cm}^2\text{V}^{-1}\text{s}^{-1}$ at 9 GHz.

2.3. The Origin of Carrier Localization

For the probed CuFeO_2 sample, the carrier localization can satisfactorily be explained by the presence of electro-statically charged boundaries of the crystallographic domains that coherently scatter X-rays. The grazing incidence X-ray diffraction (GIXRD) pattern in Figure 1c shows mainly the CuFeO_2 phase with only very minor CuFe_2O_4 and Fe_3O_4 phase contributions. Further, a substantial broadening of the XRD peaks, relative to the instrument resolution, can be observed. Modeling with Le Bail refinement^[92–94] reveals an anisotropic XRD domain size of 19 nm along the c -axis and < 12 nm along the a/b axes. As recently shown for CeO_2 , such grain boundaries can be electrostatic barriers, which decrease toward the crystallite interior as illustrated in Figure 1d.^[42] The barrier width is usually in the order of the Debye length $\lambda_D = \sqrt{\epsilon k_B T / n e^2}$, which is ≈ 5 nm for CuFeO_2 based on the reported carrier concentration n of $\approx 10^{18} \text{ cm}^{-3}$ ^[22] and a relative permittivity ϵ of ≈ 20 .^[43] Considering the average XRD domain of 14 nm, carriers are expected to localize within ≈ 4 nm, which roughly agrees with the localization length of 1.5 nm determined using the mDS-model. The small discrepancy may also be caused by the difference between the step-like barrier profiles of the mDS-model and a more realistic smooth electrostatic barrier as illustrated in Figure 1d.

In general, the possible origins of carrier localization in metal oxides are manifold and may vary between individual materials. However, the determined localization length of a few nanometers reduces these possibilities. Figure 2 illustrates possible simultaneous partial localization on different length scales and indicates which kinds of localization may be responsible for the offset between the mobilities at 1 THz and 9 GHz, which are probed by OPTP and TRMC respectively.

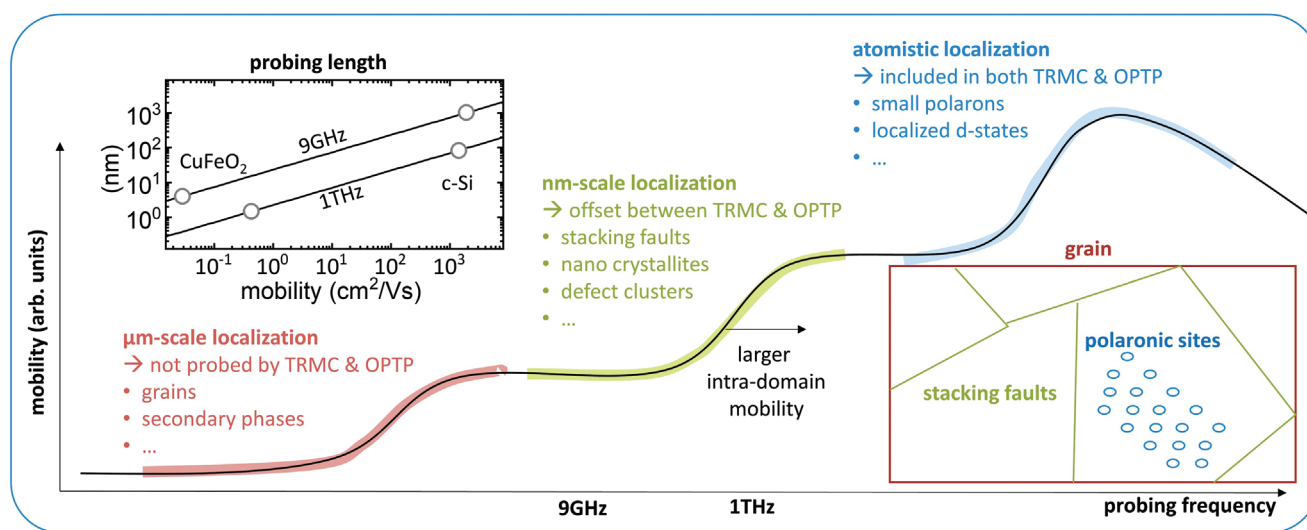


Figure 2. Localization on multiple length scales. Scheme of the frequency-dependent mobility for multiple partial localization processes on different length scales that are possible in metal oxides and an illustration of a μm -sized grain that is subdivided by stacking faults and polaron hopping between the lattice sites. The offset between THz and GHz mobilities is usually caused by nanometer-scale localization. But the mobility dispersion shifts for larger intra-domain mobilities to higher frequencies and the offset between GHz and THz mobilities becomes more sensitive to localization on longer length scales. Inset: Probing lengths for measurements at 1 THz (OPTP) and 9 GHz (TRMC) as a function of charge carrier mobility. Due to larger mobilities, the probing lengths are much longer for crystalline silicon (c-Si) than for CuFeO_2 .

Small polaron formation, trapping into localized d-states, or trapping into defect states have been reported for metal oxides. However, these processes localize the carriers on single lattice sites and the corresponding localization length should be on the atomistic scale. Therefore, they can be out-ruled as the origin of the observed nanometer-scale localization. Still, some of these atomistic localization processes possibly occur in CuFeO₂ and may be responsible for a mobility dispersion at higher frequencies as illustrated in Figure 2.

The observed offset between THz and GHz mobilities and the corresponding nanometer-scale localization may be caused by electrostatically charged grain boundaries, crystallographic twins, or stacking faults as suggested by the XRD domains size, but also by, for example, defect clusters.

Larger domains in CuFeO₂, such as micrometer-sized grains or secondary phase inclusions, are not probed by TRMC nor by OPTP.

Although the offset between the mobilities at 1 THz and 9 GHz is caused in the case of CuFeO₂ by localization on a few nanometers. In general, such an offset may be caused by localization on different length scales for materials with different mobility. Therefore, it is important to explicitly calculate the localization length or the probing lengths of TRMC and OPTP.

2.4. The Probing Lengths of TRMC and OPTP

The probing length L_{probe} is the distance over which charge transport is probed (by TRMC or OPTP) and is derived here by considering the mDS-model of a hypothetical additional localization. The mDS-model could only predict a mobility reduction by carrier localization if the probing length is larger than the localization domain size. Here we define the probing length to be equal to the domain size (localization length) that would reduce the effective mobility $\mu(f)$ in the mDS-model to half of the intra-domain value, which yields Equation 3 as derived in SI-2 (Supporting Information). Different definitions for the “starting point” of this reduction, such as a mobility reduction to 90%, lead to probing lengths with different pre-factors than in Equation 3.^[36] The resulting probing length is a function of mobility and probing frequency. High charge carrier mobilities will increase the probing length, while higher frequencies reduce it.

$$L_{\text{probe}} \approx \sqrt{\frac{6k_{\text{B}}T\mu(f)}{\pi ef}} \quad (3)$$

For total localization ($c = 1$), the probing length equals the localization length L_{loc} of the mDS-model, as shown in SI-1 (Supporting Information). For partial localization, the corresponding length should lie between the OPTP probing length and the TRMC probing length, which allows estimating the localization length from these probing lengths without modeling the full mobility dispersion.

For CuFeO₂, the OPTP-derived mobility of 0.43 cm²V⁻¹s⁻¹ at $f \approx 1$ THz yields a probing length L_{probe} of 1.5 nm. Assuming the same mobility at the lower TRMC frequency of ≈ 9 GHz would result in a \approx ten times larger (square root of 1 THz

over 9 GHz) probed transport distance of ≈ 17 nm. However, carrier localization reduces the mobility at 9 GHz to 0.029 cm²V⁻¹s⁻¹ and limits the TRMC probing length to only ≈ 4.1 nm. For other materials with higher mobilities, for example, lead halide perovskites 30 cm²V⁻¹s⁻¹ or crystalline silicon 1930 cm²V⁻¹s⁻¹, the larger THz/GHz probing length of 12/130 and 70/1060 nm are obtained, as shown in the inset of Figure 2.

In conclusion, the combination of TRMC and OPTP measurements only reveals carrier localization for which the localization length is in between the probing lengths of TRMC and OPTP.

2.5. Kinetics of Localization and Recombination

Interpreting the kinetics of the combined photoconductivity transient of CuFeO₂, which is shown for convenience again in Figure 3a, is challenging since multiple processes occur on similar timescales. Still, we discuss the main processes in analogy to the results reported for other metal oxides and in particular in comparison with BiVO₄ for which nanometer-scale localization is absent.

This absence becomes evident from the match between TRMC and OPTP transients without offset that we observed previously and is shown here in Figure 3b again.^[28] The large crystallite size can rationalize the absence of nanometer-scale localization in BiVO₄. X-ray diffraction patterns and electron backscattering (EBSD) diffraction maps of PLD-made samples are shown in the supporting Figure S2a,c (Supporting Information). They yield XRD domain sizes of >100 nm (close to the resolution limit), and a mean EBDS domain size of 1.4 μ m, which are both much larger than the obtained diffusion length. To understand if the observation above is specific to the PLD-grown BiVO₄, a BiVO₄ thin film grown by spray pyrolysis was probed and the results are shown in the supporting Figure S1 (Supporting Information). Therefore, BiVO₄ tends not to show nm-scale localization, regardless of the deposition technique. Still, localization on smaller (e.g., atomic) lengths does occur in BiVO₄.

Initially, carriers are photogenerated in CuFeO₂ and BiVO₄ with high excess energy into states that have usually very low mobilities. Then carriers thermalize and relax to the mobile band edges, which causes the initial rise of the photoconductivity in Figure 3a and corresponds to an increase in the effective charge carrier mobility.^[44] Subsequently, a steep decay within the first ps follows for CuFeO₂. This decay is at least partially caused by the localization of carriers on the nanometer scale, which is evident from the terahertz mobility spectrum measured at 5 ps (Figure 1b). The initial decay of BiVO₄ is less pronounced, which can also be explained by the absence of nanometer localization in BiVO₄. For both materials, other additional localization processes may occur. For example, (multiple) trapping into defects or band tails as previously described for BiVO₄ and TiO₂,^[45–47] exciton formation as known for ZnO,^[48] and polaron formation that is reported for BiVO₄ and α -Fe₂O₃.^[49–51] At the time of the peak of the photoconductivity transient, likely only a minor fraction of the carrier is in the high mobility band edges states and large fractions are still in

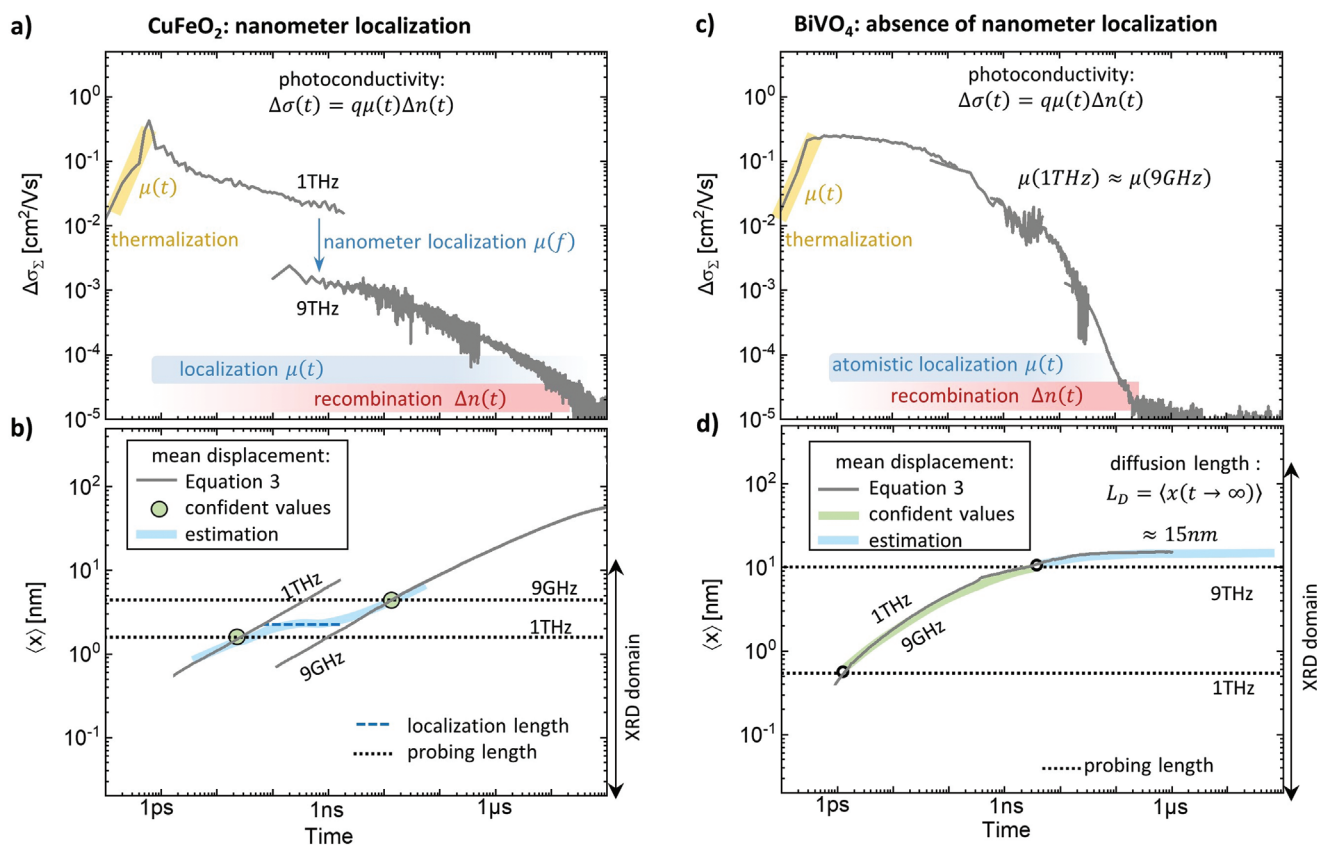


Figure 3. Localization versus homogeneous diffusion. a) Stitching photoconductivity transients to the OPTP value and to the lower TRMC value for CuFeO₂ yields different combined transients due to the carrier localization. b) Mean displacement calculated by Equation 4 for the photoconductivity plotted in a. The mean displacement reaches the OPTP probing length of 1.5 nm after 23 ps and the TRMC probing length of 4 nm after 11 ns. In between these times, the mean displacement is estimated to be limited by the localization length. For much longer times, the mean displacement is overestimated by Equation 4 as TRMC or OPTP does not probe possible additional large-scale localization. c) Stitching photoconductivity transients to the OPTP value and to the TRMC value for BiVO₄ yields similar combined transients without a significant offset in the mobilities as reported earlier.^[28] d) The mean displacement calculated by Equation 4 from the photoconductivity transient plotted in c. The evolution of the mean displacement can be stated confidently between the probing lengths of OPTP and TRMC of 1.1 nm and 12 nm, respectively. After ≈10 ns, the mean displacement estimated by Equation 4 converges to a diffusion length of 15 nm.

higher band states or already in localized states, which explains the relatively low THz peak mobility. In general, the localization processes are connected to a decay in the average mobility of the photogenerated carriers. On the longer timescales, recombination should become more significant, which decreases the photoconductivity by a decay of the carrier concentration. However, localization and recombination cannot be distinguished here.

Compared to BiVO₄, the photoconductivity tail of the CuFeO₂ photoconductivity transient is extraordinarily long. This behavior suggests that the lifetimes of some carriers are relatively long (up to 100 μs), which is often taken as a sign of a good photoabsorber.^[25] However, in this case, the long decay time is rather a consequence of carrier localization or trapping. Here, it will be interpreted in the framework of the observed carrier localization in crystallographic domains. On the one hand, the recombination centers are potentially located at the domain boundaries or in specific defect-rich domains. Hence, they cannot be reached easily by the charge carriers due to the barriers at the domain boundaries. Additionally, electrons and holes tend to localize at different posi-

tions in a potential landscape, which further increases the apparent lifetime. On the other hand, the localization will prevent carriers from reaching selective contacts or the electrolyte interface, which opposes the charge separation and slows the electrochemical reactions when used in a photoelectrochemical device.^[52] To reach the interface, the carriers must overcome the localization barrier, simultaneously exposing them to the recombination centers.

In a similar manner, charge carriers can localize by trapping into defects, band tails, or polaronic states, which also can prevent them from reaching recombination centers and causes slow decay components.^[53–56] Such atomistic localization is a likely explanation for the long decay components in BiVO₄ where nanometer-scale localization is absent. It may similarly affect the kinetics in CuFeO₂ although this is not evident from our measurements.

Anyway, the reduced transport and the relatively long lifetime likely have the same origin and partially balance each other in their effect on the diffusion length. Thus, we conclude that long-lived tails of the photoconductivity transients are not necessarily a sign of a good photoabsorber.

2.6. Ambiguous Diffusion Length

For cases in which the charge carriers are subject to time-dependent lifetimes and time-dependent mobilities and in which the individual physical processes involved might be challenging to deconvolute, we have recently derived an equation for determining the diffusion length.

The mean absolute displacement $\langle |x(t)| \rangle$ and the diffusion length L_D can be calculated by Equation 4 directly from the integral of sheet photoconductivity transients $\Delta\sigma_{\Sigma}(t')$, which are measured by TRMC and OPTP,^[28] and from the initially induced sheet carrier concentration $\Delta n_s(t' = 0)$. The mean displacement converges to the diffusion length at sufficiently long times, that is, $L_D = \langle |x(t \rightarrow \infty)| \rangle$. As TRMC and OPTP measure the sum of the photoconductivities induced by electrons and holes, the mean displacement and the diffusion lengths calculated by Equation 3 are effective values assuming equal electron and hole mobilities.

$$\langle |x(t)| \rangle \approx 0.75 \sqrt{2} \int_0^t \frac{\Delta\sigma_{\Sigma}(t')}{\Delta n_s(t' = 0)} \frac{k_B T}{e^2} dt' \quad (4)$$

In our previous work on PLD-grown BiVO₄, halide perovskites, amorphous silicon thin films, and a crystalline silicon wafer,^[28] the mean displacements calculated by Equation 4 converged to finite diffusion lengths, which were in line with literature data from other techniques. However, these materials did not exhibit carrier localization between the TRMC probing and OPTP probing lengths.

In contrast, the carrier localization and the mobility dispersion observed for CuFeO₂ in Figure 1 conflict with Equation 4, which assumes that the mobility is homogeneous throughout the medium and frequency-independent. Stitching the photoconductivity transients to either the TRMC transient measured at 9 GHz or the OPTP transient measured at 1 THz yields two different combined transients. Consequently, applying Equation 4 to both transients leads to ambiguous values for the mean displacements, as shown in Figure 3b. The only two values that can be stated with confidence are the times at which the mean displacements approach the corresponding probing lengths (green markers in Figure 3b). For CuFeO₂, it takes 23 ps and 11 ns for the carriers to spread 1.5 nm and 4 nm. In between these times, the mean displacement increases significantly slower than expected for conventional diffusion ($\approx t^{0.5}$), which can be attributed to the partial carrier localization. Likely, the mean displacement is limited by the localization length until a part of the carriers overcome the localizing barriers.

Mean displacements and diffusion lengths beyond the probing lengths of TRMC disregard possible additional transport barriers on longer length scales that may limit long-range transport. Hence, the calculated mean displacements do not converge to a finite diffusion length but continuously increase even after 100 μ s in Figure 3b, are likely overestimated. Mean displacements that are shorter than the probing lengths of OPTP are potentially underestimated as such transport may not be affected by the barriers that are probed by OPTP. Only measurements at lower or higher frequencies will allow probing

carrier transport and potential localization on such longer or shorter length scales.

For BiVO₄, the probing lengths of ≈ 11 nm for TRMC and ≈ 1.1 nm for OPTP are indicated by dotted lines in Figure 3d. Since the transients and the corresponding mean displacement 9 GHz and 1 THz coincide, the mean displacements between the probing length can be stated with confidence. Also, the diffusion length can be estimated, since the mean displacement converges. In conclusion, due to carrier localization and the corresponding mobility dispersion, the diffusion length cannot be determined unambiguously but only the times at which probing lengths are approached.

3. Screening Photo-Absorbing Metal Oxides

Having shown two main distinct behaviors for CuFeO₂ and BiVO₄, we further screened various metal oxide thin films, including α -Fe₂O₃, FeVO₄, α -SnWO₄, CuBi₂O₄, and BaSnO₃. The latter four are emerging photoelectrode materials in the field of solar fuels (Deposition details are found in the Supporting Information^{86–92}). The initial THz peak mobilities of the metal oxides under investigation are shown in Figure 4a. All values remain < 2.6 cm²V⁻¹s⁻¹, and most of them are in the order of ≈ 0.3 cm²V⁻¹s⁻¹. These values are at least one order of magnitude below the mobility of inorganic or hybrid materials that yield high-efficiency solar cells, such as halide perovskites (≈ 30 cm²V⁻¹s⁻¹), crystalline silicon (≈ 1000 cm²V⁻¹s⁻¹) or InP (≈ 2000 cm²V⁻¹s⁻¹).^[36] They are relatively comparable to those known for well-performing organic PV materials (≈ 0.4 cm²V⁻¹s⁻¹).^[57] Organic solar cells recently surpassed 19% efficiency,^[58] showing that such low mobilities are no fundamental limitation but require sophisticated device architectures.^[59]

The reason for this common low THz mobility of metal oxides could be carrier localization on length scales below the THz probing length of a few nanometers. Such localization on the atomic scale has been reported for metal oxides, for example, due to small polaron formation in BiVO₄^[49–51,63] intrinsically localized d-states in α -Fe₂O₃^[60–62] or trapping in defect states. Hence, even for BiVO₄, which does not exhibit carrier localization on the nanometer scale, carrier localization on the atomistic scale is not excluded but actually reported.^[49,55]

It can be observed in Figure 4a that apart from BiVO₄, all the probed metal oxides in this study exhibit lower mobilities at 9 GHz than at 1 THz, which can be attributed to carrier localization on the nm-length scale. To correct previous reports of some of the authors of this study, the TRMC-derived peak mobilities are also shown in Figure 4a, which are significantly lower than the previous values that were based on an incorrect analysis (SI-3, Table S2, Supporting Information). The correctly determined TRMC-derived peak mobilities are significantly lower than the initial mobilities at 9 GHz due to the photoconductivity decay within the time resolution of the conventional TRMC setup. The ratio of mobilities at 9 GHz and 1 THz is represented by the blue area in Figure 4a. It is a measure of the strength of the carrier localization and allows defining the localization strength $c^* = 1 - \mu(9\text{GHz})/\mu(1\text{THz})$, which is similar (but not equal) to the localization strength c of the mDS-model. For a straightforward comparison between different materials,

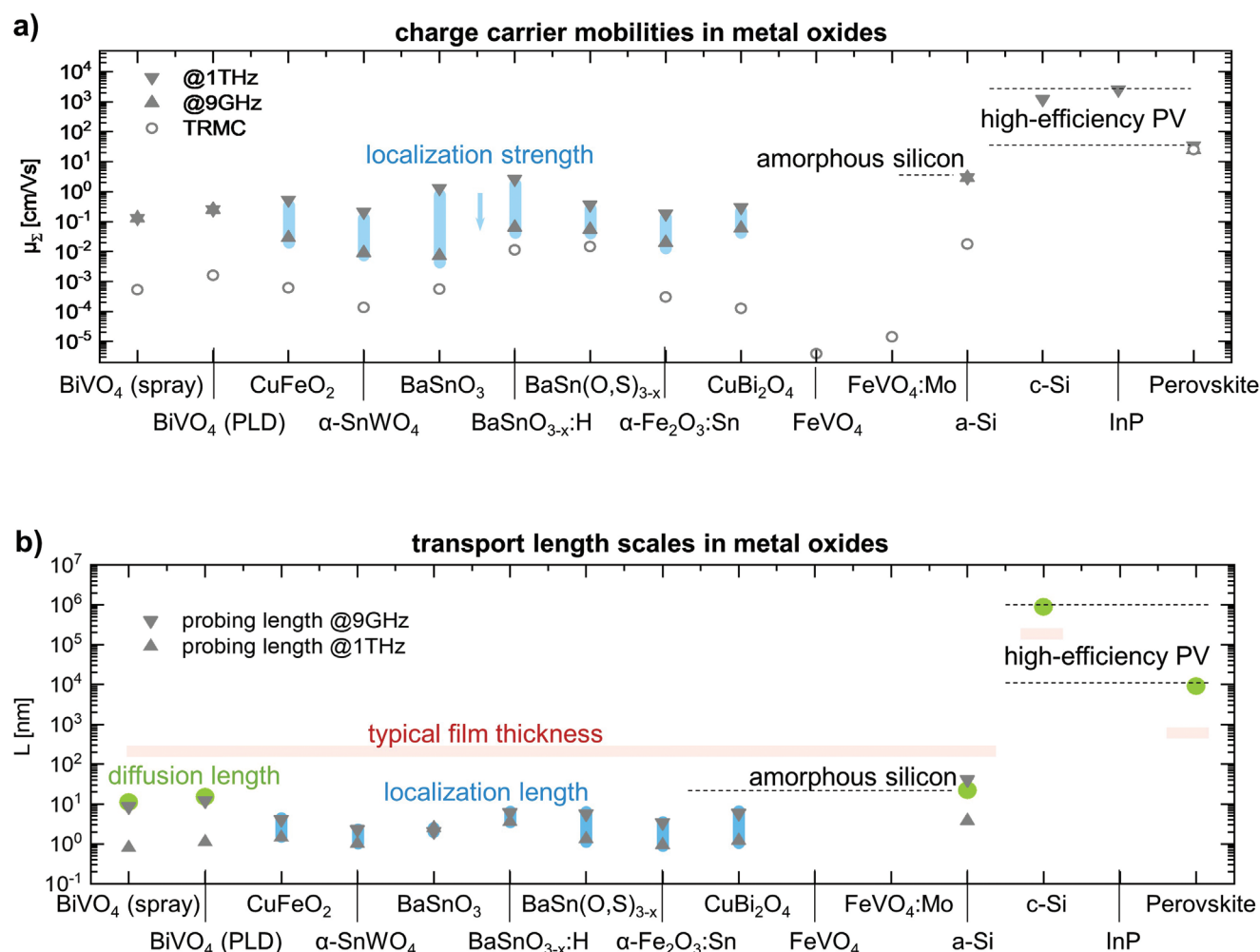


Figure 4. Screening metal oxides. a) Sum mobilities in several metal oxide photoelectrode materials are significantly lower than in high-efficiency PV materials and even lower than in amorphous silicon, indicating intrinsically slow transport. The mobility reduction from 1 THz to 9 GHz is caused by carrier localization, and its amplitude quantifies the localization strength. A photoconductivity decay within the TRMC time resolution causes even lower TRMC peak mobilities. b) The transport length scales can be quantified by the diffusion length or, if carrier localization occurs, by the localization length, which is in between the probing lengths at 9 GHz (TRMC) and at 1 THz (OPTP). For metal oxides, these transport lengths are shorter than the desired layer thickness, which will cause losses in the corresponding power conversion devices.

we will use the simplified localization parameter c^* , as it can be determined directly from the OPTP and TRMC transients. In contrast, a precise fitting of the mDS-model requires an additional measurement of the frequency-dependent THz mobility spectra. The values of c^* for all metal oxides are given in Table 1 together with the probing lengths and the peak mobilities for OPTP and TRMC, respectively. The determined localization strengths show that the charge transport in all probed metal oxides, apart from BiVO₄, suffers from carrier localization.

The transport length scales in the various metal oxides are shown in Figure 4b. The diffusion lengths could only be calculated for BiVO₄ and for the reference materials silicon and lead halide perovskite. For the other metal oxides (Figure S4, Supporting Information), the calculated mean displacements do not converge. This is unlikely to represent the actual behavior but is an artifact from the carrier localization and the potentially lower mobilities at length scales longer than the transport lengths probed by TRMC and OPTP. For the metal oxides

with carrier localization, the probing lengths are in the range 1–6 nm and the localization lengths are between these probing lengths, marked by the blue range in Figure 4b.

Overall, the localization-free transport in BiVO₄ is quantified by a diffusion length of 15 nm, and the localized transport in the other metal oxides is quantified by the localization lengths in the range 1–6 nm. Both transport lengths are much shorter than the typical layer thickness of a few hundred nanometers needed to absorb enough solar photons in an energy conversion device. Hence, carrier transport in metal oxides, and in particular the carrier localization, should be optimized or transport must be enhanced by electric fields. In comparison, for high-efficiency PV materials, such as silicon and halide perovskites, the calculated diffusion lengths are much larger than the typical layer thicknesses, resulting in no significant current losses from carrier transport.

In this context, it is notable that the only metal oxide investigated in this work that exhibits no signs of carrier localization

Table 1. Overview of obtained transport properties of emerging metal oxides.

	Diffusion length [nm]	Localization strength c^*	Probing length @1 THz [nm]	Probing length @9 GHz [nm]	Peak mobility @1 THz [$\text{cm}^2\text{V}^{-1}\text{s}^{-1}$]	Peak mobility @9 GHz [$\text{cm}^2\text{V}^{-1}\text{s}^{-1}$]	Peak mobility TRMC [$\text{cm}^2\text{V}^{-1}\text{s}^{-1}$]
BiVO_4 (PLD)	14	0	1.1	12.0	0.25	0.25	1.6×10^{-3}
BiVO_4 (spray)	11	0	0.8	8.7	0.13	0.13	5.4×10^{-4}
a-Si	22	0	3.8	41	2.9	2.9	1.8×10^{-2}
CuFeO_2	artificial divergence	0.93	1.46	4.1	0.43	0.029	6.2×10^{-4}
$\alpha\text{-SnWO}_4$	"	0.96	1.0	2.3	0.21	0.0092	1.3×10^{-4}
BaSnO_3	"	0.99	2.5	2.1	1.3	0.0073	5.6×10^{-4}
$\text{BaSnO}_{3-x}:\text{H}$	"	0.97	3.6	6.1	2.6	0.064	1.1×10^{-2}
$\text{BaSn}(\text{O},\text{S})_{3-x}$	"	0.85	1.3	5.7	0.36	0.055	1.5×10^{-2}
$\alpha\text{-Fe}_2\text{O}_3:\text{Sn}$	"	0.89	0.94	3.4	0.18	0.020	3×10^{-4}
CuBi_2O_4	"	0.80	1.2	5.9	0.30	0.06	1.3×10^{-4}
FeVO_4	–	–	–	4.1	no signal	–	3.9×10^{-6}
$\text{FeVO}_4:\text{Mo}$	–	–	–	2.3	no signal	–	1.4×10^{-5}
uncertainty	$\pm 25\%$	$\pm 50\%$	$\pm 25\%$	$\pm 25\%$	$\pm 25\%$	$\pm 50\%$	$\pm 25\%$

on the nanometer scale is BiVO_4 , which is one of the metal oxides for solar PEC water splitting with the highest reported EQE values. Hence, we suspect that the absence of nm-scale localization due to, for example, grain boundaries is an essential prerequisite for a metal oxide to achieve high solar conversion efficiencies. While improving the microstructure consequently showed increased extractable photocurrents in SnWO_4 ,^[33,64] FeVO_4 ,^[65] and CuBi_2O_4 ,^[66] photoelectrodes, this is still yet to be realized in many emerging metal oxides.

In contrast, the probed $\alpha\text{-Fe}_2\text{O}_3$ was grown epitaxially so that the microstructure should not restrict the transport. Hence, the observed nanometer-scale localization must have a different origin, for example, defect clusters, but clarifying the exact origin needs more detailed studies. The reported localization on the d-states can be out-ruled as the origin of the observed nanometer-scale localization since the corresponding localization length should be on the atomistic scale. A previous study has shown that TRMC photoconductivity measurements do not detect carriers in such d-states, which indicates atomistic localization without considerable transport between the d-states.^[60]

From the selection of novel materials investigated here, the localization is strongest for BaSnO_3 with a mobility reduction from 1.3 to $0.007 \text{ cm}^2\text{V}^{-1}\text{s}^{-1}$. Interestingly, annealing in H_2 and H_2S at 400 °C reduces the localization strength (blue bar in Figure 4a) and increases the localization length from ≈ 2 to ≈ 6 nm. This reduction of carrier localization strength rationalizes our previously reported increase of TRMC-derived mobility.^[67] Future work will clarify if an increasing XRD domain size is responsible for this reduced localization as in CuFeO_2 , or if the annealing in a reducing atmosphere introduces extended defect bands of oxygen vacancies as suggested in references,^[67–70] which would allow relatively fast transport. In the latter case, the localization length may correspond to the size of the defect clusters. Nonetheless, this example shows that carrier localization can in some cases be effectively reduced. Overcoming it should allow long-range transport with a mobility value approaching that derived from OPTP, which is $2.6 \text{ cm}^2\text{V}^{-1}\text{s}^{-1}$ for hydrogen-annealed BaSnO_3 and much larger

than for any other metal oxide probed here. This high mobility is in line with one of the smallest effective masses reported for a metal oxide so far.^[71] Therefore, this material seems to be promising despite the observed carrier localization.^[72–75]

On the other side, FeVO_4 exhibits especially poor transport since the TRMC amplitude is the lowest, and the OPTP signal was too small to be monitored and remained buried in the noise. For this material, the mobility is likely intrinsically limited by atomistic localization on iron d5-states to very low values, even without additional localization on the nanometer scale.^[77]

4. Conclusion

In this work, we combined TRMC and OPTP transients to measure the mobilities of photogenerated charge carriers and to monitor their photoconductivity and diffusion from 100 fs to the μs -regime. Particularly for CuFeO_2 , $\alpha\text{-Fe}_2\text{O}_3$, $\alpha\text{-SnWO}_4$, CuBi_2O_4 , and BaSnO_3 , frequently discussed atomistic carrier localization such as small polaron formation, trapping into point defects, or intrinsically localized d-states, are not limiting the transport through the probed thin film materials at their status of material development. Instead, transport is limited by partial carrier localization at a typical length scale of a few nm, which seems to be a common issue of metal oxide photoabsorbers. This localization occurs within a few picoseconds and leads to extraordinarily slow decay components of up to 100 μs in photoconductivity transients. Such long tails can lead to an overestimation of the carrier diffusion and are not automatically a sign of a good photoabsorber. Another fingerprint of carrier localization is the offset between OPTP and TRMC-derived transient, which reflects a reduction of the mobility at ≈ 9 GHz, probed by TRMC, compared to the mobility at ≈ 1 THz, probed by OPTP. This frequency-dependence opposes the determination of the diffusion length but allows quantifying the localization length instead. From a methodological perspective, this work complements the conventional diffusion length by the determination of the probing length, the localization

strength, and the localization length. For CuFeO₂, the observed carrier localization length of 1.5 nm is in close agreement with carrier localization in the ≈14 nm-sized crystallographic domains and the expected width of electrostatically charged domain boundaries. Hence, a strategy for future improving the charge transport is increasing the crystallinity. For the other materials, the origin of the observed nanometer-scale localization remains to be clarified. However, for BaSnO₃, annealing H₂ atmosphere reduced the observed localization and increased the THz mobility to 2.6 cm²V⁻¹s⁻¹, which is the highest value of the materials studied here. Therefore, this material is a very promising candidate for the future development of a metal oxide photoabsorber with relatively high mobility.

Supporting Information

Supporting Information is available from the Wiley Online Library or from the author.

Acknowledgements

M.K., M.S., and H.H. initiated and outlined the study. M.S. performed and analyzed the TRMC, oc-TRMC, st-TRMC, and OTPP measurements. M.S. and H.H. wrote the manuscript. M.S. and H.H. designed the figures. H.H. derived Equation 3. H.H. and D.F. supervised the project. K.S. performed the COMSOL simulations of the TRMC cavity. R.G. (HZB) measured and analyzed the XRD pattern. D.A.R. and D.R.W. measured and analyzed the EBSD. R.v.d.K., supervised the contributions from his group. R.v.d.K. and D.F. secured funding for the project. M.K. prepared the BiVO₄ (PLD) and α-SnWO₄. R.P. prepared CuFeO₂. I.A. prepared the BiVO₄ (spray) and BaSnO₃. R.G. (HUJ) prepared CuBi₂O₄. A.R., and D.G. prepared the α-Fe₂O₃:Sn. M.Z. prepared the FeVO₄. All authors discussed the results and revised the manuscript. The authors acknowledge the financial support for this work from the Helmholtz International Research School “Hybrid Integrated Systems for Conversion of Solar Energy” (HI-SCORE), an initiative co-funded by the Initiative and Networking Fund of the Helmholtz Association (HIRS-0008). M.K. acknowledges funding from the German Bundesministerium für Bildung und Forschung (BMBF), project “H2Demo” (no. 03SF0619K). We acknowledge Avner Rothschild for providing lab facilities at the Technion.

Open access funding enabled and organized by Projekt DEAL.

Conflict of Interest

The authors declare no conflict of interest.

Data Availability Statement

The data that support the findings of this study are available in the supplementary material of this article.

Keywords

carrier localization, metal oxides, mobilities, photoconductivity, water splitting

Received: January 24, 2023

Revised: February 14, 2023

Published online: March 25, 2023

- [1] X. Yu, T. J. Marks, A. Facchetti, *Nat. Mater.* **2016**, *15*, 383.
- [2] M. M. Arafat, B. Dinan, S. A. Akbar, A. S. M. A. Haseeb, *Sensors* **2012**, *12*, 7207.
- [3] M. M. Rahman, A. J. S. Ahammad, J. H. Jin, S. J. Ahn, J. J. Lee, *Sensors* **2010**, *10*, 4855.
- [4] S. Navalón, A. Dhakshinamoorthy, M. Álvaro, H. Garcia, *ChemSusChem* **2013**, *6*, 562.
- [5] M. S. S. Danish, A. Bhattacharya, D. Stepanova, A. Mikhaylov, M. L. Grilli, M. Khosravy, T. Senju, *Metals* **2020**, *10*, 1.
- [6] R. Van de Krol, M. Grätzel, *Photoelectrochemical Hydrogen Production*, (Eds.: R. van de Krol, M. Grätzel), Vol. 102, Springer, Boston, MA **2012**.
- [7] K. Sivula, F. L. Formal, M. Grätzel, *Wiley-VCH Verlag*, **2011**, *4*, pp. 432–449.
- [8] W. Yang, R. R. Prabhakar, J. Tan, S. D. Tilley, J. Moon, *Chem. Soc. Rev.* **2019**, *48*, 4979.
- [9] M. Ni, M. K. H. Leung, D. Y. C. Leung, K. Sumathy, *Renew. Sustain. Energy Rev.* **2007**, *11*, 401.
- [10] J. H. Kim, J. S. Lee, *E. Environ. Focus* **2014**, *3*, 339.
- [11] Y. Chen, X. Feng, Y. Liu, X. Guan, C. Burda, L. Guo, *ACS Energy Lett.* **2020**, *5*, 844.
- [12] D. Huang, K. Wang, L. Yu, T. H. Nguyen, S. Ikeda, F. Jiang, *ACS Energy Lett.* **2018**, *3*, 1875.
- [13] L. Pan, J. H. Kim, M. T. Mayer, M. K. Son, A. Ummadisingu, J. S. Lee, A. Hagfeldt, J. Luo, M. Grätzel, *Nat. Catal.* **2018**, *1*, 412.
- [14] Y. Pihosh, I. Turkevych, K. Mawatari, J. Uemura, Y. Kazoe, *Nat. Publ. Gr.* **2015**, *5*, 1.
- [15] F. F. Abdi, S. P. Berglund, *J. Phys. D. Appl. Phys.* **2017**, *50*, 193002.
- [16] Y. Qiu, Z. Pan, H. Chen, D. Ye, L. Guo, Z. Fan, S. Yang, *Sci. Bull.* **2019**, *64*, 1348.
- [17] Y. J. Jang, J. S. Lee, *ChemSusChem* **2019**, *12*, 1835.
- [18] M. Xiao, B. Luo, Z. Wang, S. Wang, L. Wang, *Sol. RRL* **2020**, *4*, 1900509.
- [19] R. van de Krol, Y. Liang, J. Schoonman, *J. Mater. Chem.* **2008**, *18*, 2311.
- [20] A. Kay, M. Fiegenbaum-Raz, S. Müller, R. Eichberger, H. Dotan, R. van de Krol, F. F. Abdi, A. Rothschild, D. Friedrich, D. A. Grave, *Adv. Funct. Mater.* **2019**, *30*, 1901590.
- [21] M. Kölbach, I. J. Pereira, K. Harbauer, P. Plate, K. Höflich, S. P. Berglund, D. Friedrich, R. Van De Krol, F. F. Abdi, *Chem. Mater.* **2018**, *30*, 8322.
- [22] M. S. Prévot, X. A. Jeanbourquin, W. S. Bourée, F. Abdi, D. Friedrich, R. van de Krol, N. Guijarro, F. L. Formal, K. Sivula, W. S. Bouré, F. Abdi, D. Friedrich, *Chem. Mater.* **2017**, *29*, 4952.
- [23] M. Zhang, Y. Ma, D. Friedrich, R. Van De Krol, L. H. Wong, F. F. Abdi, *J. Mater. Chem. A* **2018**, *6*, 548.
- [24] M. Kölbach, K. Harbauer, K. Ellmer, R. Van De Krol, *J. Phys. Chem. C* **2020**, *124*, 4438.
- [25] R. Gottesman, I. Levine, M. Schleuning, R. Irani, D. Abou-Ras, T. Dittrich, D. Friedrich, R. van de Krol, *Adv. Energy Mater.* **2021**, *11*, 2003474.
- [26] M. Kim, B. Lee, H. Ju, J. Y. Kim, J. Kim, S. W. Lee, *Adv. Mater.* **2019**, *31*, 1903316.
- [27] Q.-L. Liu, Z.-Y. Zhao, R.-D. Zhao, J.-H. Yi, *J. Alloys Compd.* **2020**, *819*, 153032.
- [28] M. Schleuning, M. Kölbach, F. F. Abdi, K. Schwarzburg, M. Stolterfoht, R. Eichberger, R. van de Krol, D. Friedrich, H. Hempel, *PRX Energy* **2022**, *1*, 023008.
- [29] J. Shan, R. Ulbricht, M. Bonn, E. Hendry, T. F. Heinz, *Rev. Mod. Phys.* **2011**, *83*, 543.
- [30] P. Prins, F. C. Grozema, J. M. Schins, L. D. A. Siebbeles, *Phys. Status Solidi* **2006**, *243*, 382.
- [31] M. J. Bird, O. G. Reid, A. R. Cook, S. Asaoka, Y. Shibano, H. Imahori, G. Rumbles, J. R. Miller, *J. Phys. Chem. C* **2014**, *118*, 6100.
- [32] P. Kužel, H. Němec, H. Ne, *Adv. Opt. Mater.* **2020**, *8*, 1900623.
- [33] M. Kölbach, H. Hempel, K. Harbauer, M. Schleuning, A. Petsiuk, K. Höflich, V. Deinhart, D. Friedrich, R. Eichberger, F. F. Abdi, R. Van De Krol, *ACS Appl. Energy Mater.* **2020**, *3*, 4320.

- [34] N. Kopidakis, O. G. Reid, K. Zhu, G. Rumbles, M. Yang, N. Kopidakis, K. Zhu, G. Rumbles, *ACS Energy Lett.* **2016**, *1*, 561.
- [35] T. L. Cocker, D. Baillie, M. Buruma, L. V. Titova, R. D. Sydora, F. Marsiglio, F. A. Hegmann, *Phys. Rev. B* **2017**, *96*, 205439.
- [36] H. Hempel, T. J. Savenije, M. Stolterfoht, J. Neu, M. Failla, V. C. Paingad, P. Kužel, E. J. Heilweil, J. A. Spies, M. Schleuning, J. Zhao, D. Friedrich, K. Schwarzbach, L. D. A. Siebbeles, P. Dörflinger, V. Dyakonov, R. Katoh, M. J. Hong, J. G. Labram, M. Monti, E. Butler-Caddle, J. Lloyd-Hughes, M. M. Taheri, J. B. Baxter, T. J. Magnanelli, S. Luo, J. M. Cardon, S. Ardo, T. Unold, *Adv. Energy Mater.* **2022**, *12*, 2102776.
- [37] N. V. Smith, *Phys. Lett. A* **1968**, *26*, 126.
- [38] N. V. Smith, *Phys. Rev. B* **2001**, *64*, 155106.
- [39] T.-T. Kang, M. Yamamoto, M. Tanaka, A. Hashimoto, A. Yamamoto, R. Sudo, A. Noda, D. W. Liu, K. Yamamoto, *Opt. Lett.* **2009**, *34*, 2507.
- [40] J. C. Dyre, *J. Appl. Phys.* **1988**, *64*, 2456.
- [41] F. C. Grozema, L. D. A. Siebbeles, *Int. Rev. Phys. Chem.* **2008**, *27*, 87.
- [42] X. Xu, Y. Liu, J. Wang, D. Isheim, V. P. Dravid, C. Phatak, S. M. Haile, *Nat. Mater.* **2020**, *19*, 887.
- [43] T. Kimura, J. C. Lashley, A. P. Ramirez, *Phys. Rev. B* **2006**, *73*, 220401.
- [44] A. Burgos-Caminal, J. M. Moreno-Naranjo, A. R. Willauer, A. A. Paracattil, A. Ajdarzadeh, J.-E. Moser, *J. Phys. Chem. C* **2021**, *125*, 98.
- [45] R. Katoh, A. Furube, K. Yamanaka, T. Morikawa, *J. Phys. Chem. Lett.* **2010**, *1*, 3261.
- [46] Z. Meng, S. Selim, E. Pastor, A. Kafizas, J. Durrant, A. Bakulin, *Proc. SPIE* **2021**, 1179910.
- [47] E. Pastor, M. Sachs, S. Selim, J. R. Durrant, A. A. Bakulin, A. Walsh, *Nat. Rev. Mater.* **2022**, *7*, 503.
- [48] J. Kegel, I. M. Povey, M. E. Pemble, *Nano Energy* **2018**, *54*, 409.
- [49] M. Ziwrirtsch, S. Müller, H. Hempel, T. Unold, F. F. Abdi, R. van de Krol, D. Friedrich, R. Eichberger, *ACS Energy Lett.* **2016**, *1*, 888.
- [50] C. Lohaus, A. Klein, W. Jaegermann, *Nat. Commun.* **2018**, *9*, 4309.
- [51] A. J. E. Rettie, W. D. Chemelewski, D. Emin, C. B. Mullins, *J. Phys. Chem. Lett.* **2016**, *7*, 471.
- [52] M. Schleuning, I. Y. Ahmet, R. van de Krol, M. M. May, *Sustain. Energy Fuels* **2022**, *6*, 3701.
- [53] M. Kuno, D. P. Fromm, H. F. Hamann, A. Gallagher, D. J. Nesbitt, *J. Chem. Phys.* **2000**, *112*, 3117.
- [54] A. D. Wright, R. L. Milot, G. E. Eperon, H. J. Snaith, M. B. Johnston, L. M. Herz, *Adv. Funct. Mater.* **2017**, *27*, 1700860.
- [55] K. Höflich, K. Harbauer, S. P. Berglund, R. van de Krol, I. J. Pereira, M. Kölbach, P. Plate, F. F. Abdi, D. Friedrich, F. F. A. Moritz Kölbach, I. nês J.ordão Pereira, K. Harbauer, P. Plate, K. Höflich, S. P. Berglund, D. Friedrich, Roel van de Krol, *Chem. Mater.* **2018**, *30*, 8322.
- [56] P. H. Sheer, J. M. Smith, P. A. Dalgarno, R. J. Warburton, X. Chen, P. J. Dobsen, S. M. Daniels, N. L. Pickett, P. O'Brien, *Appl. Phys. Lett.* **2008**, *92*, 101111.
- [57] Z. Jin, D. Gehrig, C. Dyer-Smith, E. J. Heilweil, F. Laquai, M. Bonn, D. Turchinovich, *J. Phys. Chem. Lett.* **2014**, *5*, 3662.
- [58] J. Wang, Z. Zheng, Y. Zu, Y. Wang, X. Liu, S. Zhang, M. Zhang, J. Hou, *Adv. Mater.* **2021**, *33*, 2102787.
- [59] L. Lu, M. A. Kelly, W. You, L. Yu, *Nat. Photonics* **2015**, *9*, 491.
- [60] D. A. Grave, D. S. Ellis, Y. Piekner, M. Kölbach, H. Dotan, A. Kay, P. Schnell, R. van de Krol, F. F. Abdi, D. Friedrich, A. Rothschild, *Nat. Mater.* **2021**, *20*, 833.
- [61] Y. Piekner, H. Dotan, A. Tsyganok, K. D. Malviya, D. A. Grave, O. Kfir, A. Rothschild, *ACS Photonics* **2018**, *5*, 5068.
- [62] D. S. Ellis, R.-P. Wang, D. Wong, J. K. Cooper, C. Schulz, Y.-D. Chuang, Y. Piekner, D. A. Grave, M. Schleuning, D. Friedrich, F. M. F. de Groot, A. Rothschild, *Phys. Rev. B* **2022**, *105*, 75101.
- [63] A. J. E. Rettie, W. D. Chemelewski, J. Lindemuth, J. S. McCloy, L. G. Marshall, J. Zhou, D. Emin, C. B. Mullins, *Appl. Phys. Lett.* **2015**, *106*, 022106.
- [64] R. Gottesman, I. Peracchi, J. L. Gerke, R. Irani, F. F. Abdi, R. van de Krol, *ACS Energy Lett.* **2022**, *7*, 514.
- [65] W. Qiu, Y. Zhang, G. He, L. Chen, K. Wang, Q. Wang, W. Li, Y. Liu, J. Li, *ACS Appl. Energy Mater.* **2022**, *5*, 11732.
- [66] M. Zhang, Y. Fang, Y. F. Tay, Y. Liu, L. Wang, H. Jani, F. F. Abdi, L. H. Wong, *ACS Appl. Energy Mater.* **2022**, *5*, 3409.
- [67] C.-Y. Lin, S.-Y. Lin, M.-C. Tsai, C.-H. Wu, *Sustain. Energy Fuels* **2020**, *4*, 625.
- [68] S. Gahlawat, I. Y. Ahmet, P. Schnell, I. Levine, S. Zhang, P. P. Ingole, F. F. Abdi, *Chem. Mater.* **2021**.
- [69] S. Lee, H. Wang, P. Gopal, J. Shin, H. M. I. Jaim, X. Zhang, S.-Y. Jeong, D. Usanmaz, S. Curtarolo, M. Fornari, M. Buongiorno Nardelli, I. Takeuchi, *Chem. Mater.* **2017**, *29*, 9378.
- [70] M. Nakamura, H. Watanabe, H. Akamatsu, K. Fujii, M. Yashima, G. Hasegawa, M. Inada, K. Hayashi, K. Maeda, *Chem. Mater.* **2021**, *33*, 3631.
- [71] M. Nakamura, H. Akamatsu, K. Fujii, Y. Nambu, Y. Ikeda, T. Kanazawa, S. Nozawa, M. Yashima, K. Hayashi, K. Maeda, *Inorg. Chem.* **2022**, *61*, 6584.
- [72] G. Hautier, A. Miglio, D. Waroquiers, G.-M. Rignanese, X. Gonze, *Chem. Mater.* **2014**, *26*, 5447.
- [73] Q. Liu, J. Dai, Z. Liu, X. Zhang, G. Zhu, G. Ding, *J. Phys. D: Appl. Phys.* **2010**, *43*, 455401.
- [74] H. F. Wang, Q. Z. Liu, F. Chen, G. Y. Gao, W. Wu, X. H. Chen, *J. Appl. Phys.* **2007**, *101*, 106105.
- [75] K. T. Hong, W. Lee, C. Ju, K. Hoon, K. Char, *Appl. Phys. Express* **2012**, *5*, 8.
- [76] M. Kim, B. Lee, H. Ju, J. Y. J. Kim, J. Y. J. Kim, S. W. Lee, *Adv. Mater.* **2019**, *31*, 1903316.
- [77] T. Gro, H. Duda, J. Krok-kowalski, J. Walczak, E. Filipek, P. Tabero, A. Wyrostek, K. Barner, *Radiat. Eff. Defects Solids* **1995**, *133*, 341.
- [78] J. Neu, K. P. Regan, J. R. Swierk, C. A. Schmuttenmaer, *Appl. Phys. Lett.* **2018**, *113*, 233901.
- [79] H. Hempel, C. J. Hages, R. Eichberger, I. Repins, T. Unold, *Sci. Rep.* **2018**, *8*.
- [80] T. J. Savenije, A. J. Ferguson, N. Kopidakis, G. Rumbles, **2013**, *J. oPhys. Chem. C* *117*, 24085.
- [81] P. P. Infelta, M. P. de Haas, J. M. T. Warman, *Rad. Phys. and Chemistry* **1977**, *10*, 353.
- [82] T. J. Savenije, A. J. Ferguson, N. Kopidakis, G. Rumbles, *J. Phys. Chem. C* **2013**, *117*, 24085.
- [83] O. G. Reid, D. T. Moore, Z. Li, D. Zhao, Y. Yan, K. Zhu, G. Rumbles, *J. Phys. D: Appl. Phys.* **2017**, *50*, 493002.
- [84] F. F. Abdi, N. Firet, R. van de Krol, *ChemCatChem* **2012**, *5*, 490.
- [85] I. Y. Ahmet, Y. Ma, J.-W. Jang, T. Henschel, B. Stannowski, T. Lopes, A. Vilanova, A. Mendes, F. F. Abdi, R. van de Krol, *Sustain. Energy & Fuels* **2019**, *3*, 2366.
- [86] M. A. Zurbuchen, J. Lettieri, S. J. Fulk, Y. Jia, A. H. Carim, D. G. Schlom, S. K. Streiffer, *Appl. Phys. Lett.* **2003**, *82*, 4711.
- [87] A. Kay, D. A. Grave, D. S. Ellis, H. Dotan, A. Rothschild, *ACS Energy Lett.* **2016**, *1*, 827.
- [88] J.-W. Jang, D. Friedrich, S. Müller, M. Lamers, H. Hempel, S. Lardhi, Z. Cao, M. Harb, L. Cavallo, R. Heller, R. Eichberger, R. van de Krol, F. F. Abdi, *Adv. Energy Mater.* **2017**, *7*, 1701536. Portico.
- [89] M. Lamers, S. Fiechter, D. Friedrich, F. F. Abdi, R. J. van de Krol, *Mat. Chem. A* **2018**, *6*, 18694.
- [90] S. P. Berglund, F. F. Abdi, P. Bogdanoff, A. Chemseddine, D. Friedrich, R. van de Krol, *Chem. Mater.* **2016**, *28*, 4231.
- [91] F. Wang, W. Septina, A. Chemseddine, F. F. Abdi, D. Friedrich, P. Bogdanoff, R. van de Krol, S. D. Tilley, S. P. Berglund, *J. Am. Chem. Soc.* **2017**, *139*, 15094.
- [92] A. Le Bail, H. Duroy, J. L. Fourquet, *Mater. Res. Bull.* **1988**, *23*, 447.
- [93] P. Thompson, D. E. Cox, J. B. Hastings, *J. Appl. Crystallogr.* **1987**, *20*, 79.
- [94] Rodríguez-Carvajal, Juan. "An introduction to the program FullProf." Laboratoire Leon Brillouin (CEA-CNRS), **2001**.